Chemical Engineering Science 312 (2025) 121655

Contents lists available at ScienceDirect

Chemical Engineering Science

journal homepage: www.elsevier.com/locate/ces

Kinetic modeling and conceptual design of the OME synthesis from trioxane and dimethyl ether on H-ZSM-5

Bruno Lacerda de Oliveira Campos *, Philipp Beeskow, Marius Drexler, Karla Herrera Delgado, Ulrich Arnold, Jörg Sauer

Institute for Catalysis Research and Technology (IKFT), Karlsruhe Institute of Technology (KIT), Hermann-von-Helmholtz-Platz 1, D-76344 Eggenstein-Leopoldshafen, Germany

ARTICLE INFO

Keywords:
Reaction kinetics
OME synthesis
Trioxane
Dimethyl ether
H-ZSM-5
Conceptual design

ABSTRACT

This work presents a new nine-parameter kinetic model for the synthesis of oxymethylene ethers (OME) from dimethyl ether (DME) and trioxane (TRI) on the zeolite H-ZSM-5 (Si/Al = 40), which according to recent studies is an active and selective catalyst for this reaction. To establish a database for model parametrization, experiments covering a relevant operating window were performed in a batch reactor with periodic sampling (at 353–393 K and a TRI/DME molar ratio in feed of 0.25–0.70). In addition, the database was enlarged with experiments from a previous work. The model accurately reproduced the data, and the simulations suggest that the direct incorporation of TRI to form OME_3 is the preferred reaction pathway for OME production. Furthermore, an optimal operating window was identified considering the trade-off between catalyst activity and OME selectivity. Finally, a conceptual process design for continuous OME production from DME and TRI is proposed.

1. Introduction

Oxymethylene ethers (OME) are an interesting alternative to fossil diesel fuel, because it can be produced from renewable sources and has favorable combustion characteristics in terms of emission profile. The chemical formula of OME is $CH_3O(CH_2O)_nCH_3$, with the physicochemical properties of $OME_{n=3-5}$ being close to those of conventional diesel fuels (Deutsch et al., 2017; Omari et al., 2019). Taking into account the required stability at the low temperatures of a rigorous winter, OME_{3-4} in particular can be used in diesel blends with the current fleet, or as pure fuels with minor modifications in the vehicle (Liu et al., 2017). Due to the absence of C-C bonds in the molecular structure, the formation of soot particles is strongly suppressed, similar to C_1 fuels (Gelner et al., 2022; Pélerin et al., 2020). This resolves the soot-NO_x target conflict, allowing for higher exhaust gas ratios to minimize NO_X emissions as well (Härtl et al., 2014; Holzer et al., 2022). In recent years, extensive research has focused on novel, cost-efficient routes for OME synthesis, some of which have been scaled up to pilot scale (Mantei et al., 2023; Voggenreiter et al., 2022). In addition, modifications of the OME structure have been explored to tune desired physicochemical properties (An et al., 2022; Bartholet et al., 2021; Drexler et al., 2021; Lucas et al., 2022), opening up opportunities for these compounds to be used as fuel additives or in other applications in the chemical industry.

In anhydrous OME production processes, which are more selective than the aqueous processes (Oestreich et al., 2018; Voggenreiter and Burger, 2021), typical reactants are trioxane (TRI) and OME_1, with the reaction being catalyzed by acidic materials, such as zeolites or ion-exchange resins. An emerging approach is to substitute OME_1 for dimethyl ether (DME), which can be produced on a large scale directly from syngas, thereby reducing process costs (Drexler et al., 2023). The only byproduct of OME synthesis from DME and TRI is methyl formate (MeFo), which is considered an attractive candidate to substitute gasoline fuel (Maier et al., 2019). In catalyst screening studies, the zeolite H-ZSM-5 (Si/Al = 40) exhibited high activity and high OME selectivity in the DME/TRI system, outperforming a variety of catalytic systems (Drexler et al., 2022; Drexler et al., 2023). Furthermore, the feasibility of a gas-phase OME synthesis process based on DME and monomeric formaldehyde has recently been demostrated, but unfortunately the selectivity to OME was much lower compared to the liquid-phase production processes (Billion et al., 2024).

Understanding and describing the reaction kinetics is the cornerstone for process optimization and scale-up. Breitkreuz et al. investigated the kinetics of the OME synthesis from DME (Breitkreuz et al., 2022b). Two experiments with periodic sampling (type A) were conducted at 363 K with DME and TRI as feed mixture and TRI/DME molar

* Corresponding author.
E-mail address: bruno.campos@kit.edu (B. Lacerda de Oliveira Campos).

https://doi.org/10.1016/j.ces.2025.121655
Received 3 January 2025; Received in revised form 19 March 2025; Accepted 7 April 2025
Available online 10 April 2025

Nomenclature

A_i	Chromatogram integration area of component i
A_k	Lumped kinetic constant of reaction k
$A_{eq,k}$	Equilibrium constant of reaction k (–)
A_T	Parameter of the temperature profile equation (K)
a_i	Activity of component i (mol·m^{-3})
$B_{eq,k}$	Equilibrium constant of reaction k
B_T	Parameter of the temperature profile equation (K)
C_T	Parameter of the temperature profile equation (s^{-1})
$E_{A,k}$	Activation energy of reaction k (kJ·mol^{-1})
K_i	Partition coefficient of component i (–)
$K_{P,k}$	Equilibrium constant of reaction k
k_k	Kinetic constant of reaction k
M_i	Molar mass of component i (kg·mol^{-1})
m_i	Mass of component i (kg)
ME_j	Mean relative error of component j (%)
N_{TE}	Number of training experiments (–)
N_{M,E_i}	Number of measured samples of experiment E_i
n_i	Number of moles of component i (mol)
$n_{ij,x}$	Measured number of moles of point ij of component (mol)
$\hat{n}_{ij,x}$	Simulated number of moles of point ij of component x (mol)
p	Reactor pressure (Pa)
$p_{vap,i}$	Vapor pressure of component i (Pa)
RF_i	Response factor of component i
R	Universal gas constant (kJ·mol^{-1}·K^{-1})
r_k	Rate of reaction k (mol·kg$_{cat}^{-1}$·h^{-1})
S_i	Selectivity of component i with regard to trioxane (%)
T	Reactor temperature (K)
t	Time (h)
$w_{ij,x}$	Weight related to component x of point ij (–)
X_i	Conversion of component i (%)
x_i	Mole fraction of component i in the liquid phase (mol·mol^{-1})
y_i	Mole fraction of component i in the gas phase (mol·mol^{-1})
z_i	Mole fraction of component i considering the liquid and gas phases (mol·mol^{-1})
γ_i	Activity coefficient of component i (–)
v	Vapor fraction (mol·mol^{-1})
$v_{L,i}$	Molar volume of component i in the liquid phase (m^3·mol^{-1})
υ_{ik}	Stoichiometric coefficient of component i in reaction k (–)
ω_i	Weight fraction of component i (kg·kg^{-1})

Subscript

cat	Catalyst
G	Gas
init	Initial condition
L	Liquid
R	Reactor
S	Sample
tot	Total

ratio between 0.134 and 0.145, while eight experiments with periodic sampling (type B) were performed at 353–373 K with DME and different OME mixtures in the feed (including MeFo once, and always containing low amounts of trioxane). The experiments of type B were used to fit an eight-parameter model (including temperature effect). To the best of our knowledge, this is the only work in the literature on the kinetics of this reaction, in which an acidic ion-exchange resin was used as catalyst. Therefore, there is no available kinetic model describing this reaction on H-ZSM-5, which is a promising catalyst for this system.

Therefore, in the present work, a new kinetic model for the OME synthesis from DME and TRI on zeolite H-ZSM-5 (Si/Al = 40) was developed. Model parametrization and validation was performed with own experiments at 353–393 K and a TRI/DME molar ratio in feed of 0.25–0.70, a significantly wider operating window compared to the current model available in the literature (Breitkreuz et al., 2022b). Experiments without dodecane dilution from a previous study were also used to enlarge the training database. The preferential reaction pathways and an optimal operating window were identified, and a conceptual process design is proposed.

2. Experimental investigations

2.1. Catalytic tests

The zeolite catalyst H-ZSM-5 (Si/Al = 40, CBV 8014, Zeolyst International) was used as a powder. Prior to the reaction, the catalyst was calcined in air at 773 K for 3 h and dried at 383 K and 10 mbar for 12 h, as water is known to strongly inhibit OME formation and promote side reactions (Baranowski et al., 2020; Ouda et al., 2017).

Kinetic experiments were performed in a stainless-steel autoclave (50 mm inner diameter and 95 mm height). Trioxane (TRI), catalyst powder, and dodecane (as a solvent and internal standard) were put into the autoclave. The batch reactor was hermetically sealed and liquid DME was dosed using an electric syringe pump (500D, Teledyne ISCO).

Table 1
Operating conditions of the experiments performed in the batch reactor.

No.	Catalyst mass (g)	Temperature (K)	n_{TRI}/n_{DME}(mol/mol)	Initial composition (g)		
				TRI	DME	Dodecane
E1	1.291	353	0.396	22.16	28.41	49.90
E2	1.297	363	0.396	22.14	28.61	49.90
E3	1.300	373	0.402	22.16	28.61	49.80
E4	1.297	383	0.399	22.18	28.21	49.90
E5	1.297	393	0.397	22.19	28.61	49.90
E6	1.292	363	0.248	16.32	33.71	49.80
E7	1.293	383	0.250	16.34	33.41	49.80
E8	1.298	363	0.533	25.84	24.81	49.80
E9	1.298	383	0.537	25.92	24.71	49.70
E10	1.294	363	0.690	28.75	21.30	49.90
E11	1.298	383	0.692	28.84	21.30	49.90
E12	1.797	363	0.406	30.57	38.51	30.20
E13	0	393	0.396	22.14	28.61	49.90

The solution was continuously mixed with a magnetic stirrer (RCT basic, IKA), and the temperature was raised to the desired setpoint by electric heating. Temperature and pressure were monitored with a type K thermocouple and a pressure transmitter (S11, WIKA), respectively. A picture of the laboratory plant is provided in the Supplementary Material (SM, see Section S1).

Samples were taken during reaction through an opening in the reactor bottom, which was connected to two ball valves with a quarter-inch tube in between (sample volume: 1.75 mL). Each sample collection procedure was performed twice, with the first sample discarded (to flush the sampling line) and the second being collected. The collected samples were cleared of solid catalyst and solidified TRI by filtration through a syringe filter. To terminate the experiment, the autoclave was quenched in an ice water bath. A small amount of n-octane was added to the sample as reference for the gas chromatograph (GC), and the whole sample was diluted in 1:1 with tetrahydrofuran (THF).

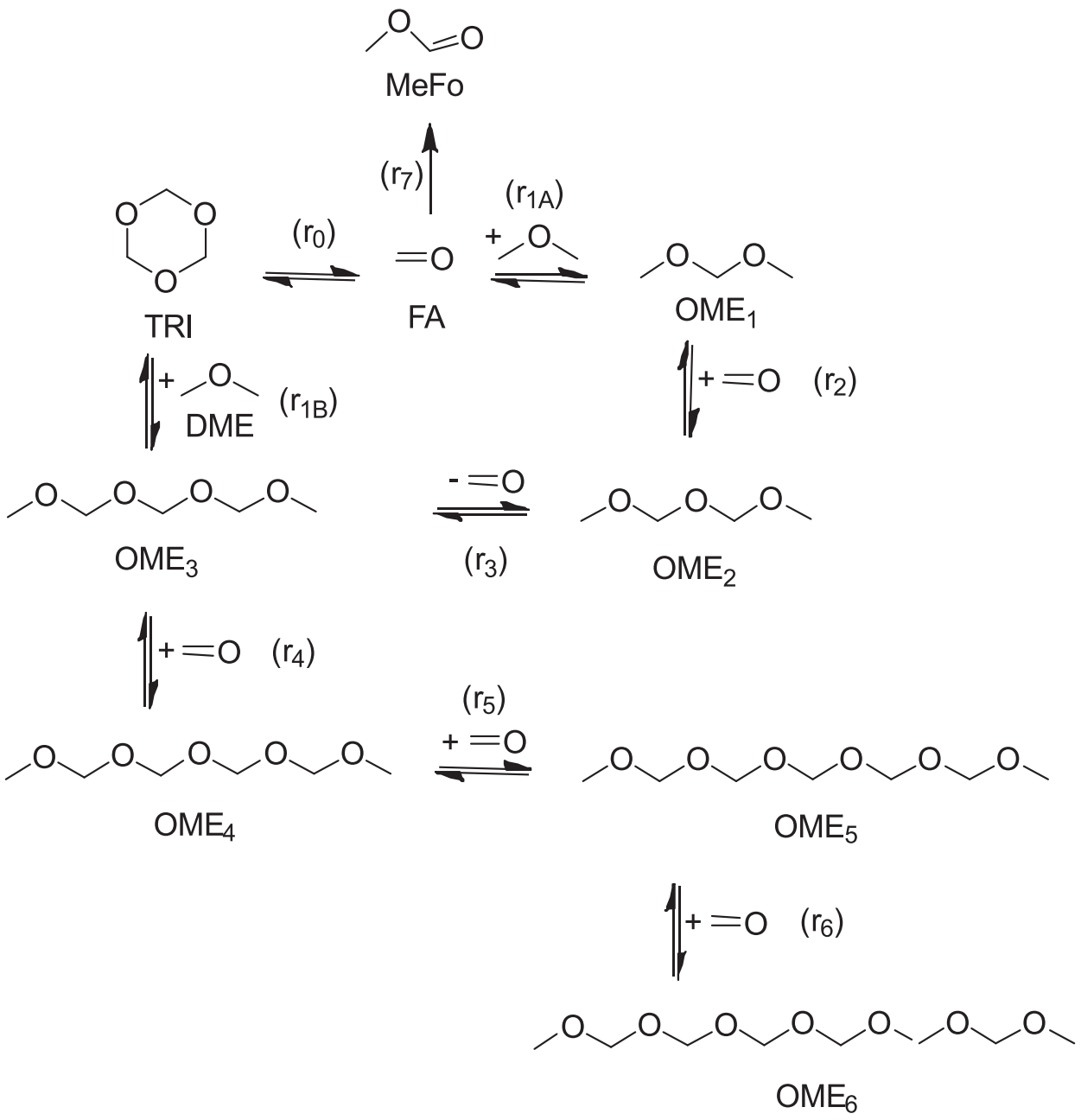

Fig. 1. Reaction network considered in the kinetic modeling. r_{1A} only belongs to Model A while r_{1B} only belongs to Model B.

The operating conditions of the experiments are summarized in Table 1. Variations in temperature and the TRI/DME ratio were applied, as well as a run with less dodecane and more catalyst (E12), and an experiment without catalyst (E13).

2.2. Analytical methods

The liquid samples were analyzed by a gas chromatograph (GC, Hewlett Packard 6890 Series), equipped with a flame ionization detector (FID), an Agilent DB-5MS + DG column, and helium as carrier gas. Pure compounds were used to determine the response factors (RF) of $OME_{1–5}$, dodecane, and MeFo. The RF of OME_6 was estimated by extrapolating the values of the other OMEs. Higher OMEs were neglected because only traces were detected.

Most of the DME evaporated during depressurization, while some TRI resolidified and was lost in the syringe filter. Therefore, although DME and TRI were indeed detected by the GC, their measured concentrations were not taken into account. Instead, these were determined by stoichiometry.

The weight fraction of dodecane in the sample ($\omega_{dod,s}$) was calculated as follows.

$$\omega_{dod,s} = RF_{dod} \bullet \frac{A_{dod} \bullet m_{oct,s}}{A_{oct} \bullet m_{tot,s}} \quad (1)$$

where A_i is the integration area in the chromatogram related to component i, $m_{oct,s}$ is the mass of octane in the sample, and $m_{tot,s}$ is the total sample mass.

Since dodecane is inert in the system, its weight fraction in the reactor remains the same as under the initial conditions ($\omega_{dod,r} = \omega_{dod,init}$). Sampling has a negligible effect on the system composition, because the liquid phase contains essentially the entire system mass (≈99.4 wt%), while the sampling mass was small (≈1.5 wt%). Thus, the weight fraction of each component in the reaction mixture ($\omega_{i,r}$) was

determined.

$$\omega_{i,r} = RF_i \bullet \frac{A_i \bullet m_{oct,s} \bullet \omega_{dod,init}}{A_{oct} \bullet m_{tot,s} \bullet \omega_{dod,s}} \tag{2}$$

The conversion of TRI (X_{TRI}) and DME (X_{DME}) and the selectivity of OME with respect to TRI (S_{OME}) were calculated as follows.

$$X_{TRI} = 100\% \bullet \frac{M_{FA}}{3 \bullet \omega_{TRI,init}} \bullet \left[\frac{2 \bullet \omega_{MeFo,r}}{M_{MeFo}} + \sum_{i=1}^{6} \left(\frac{i \bullet \omega_{OME_i,r}}{M_{OME_i}} \right) \right] \tag{3}$$

$$X_{DME} = 100\% \bullet \frac{M_{DME}}{\omega_{DME,init}} \bullet \sum_{i=1}^{6} \left(\frac{\omega_{OME_i,r}}{M_{OME_i}} \right) \tag{4}$$

$$S_{OME} = 100\% \bullet \sum_{i=1}^{6} \left(\frac{i \bullet \omega_{OME_i,r}}{M_{OME_i}} \right) \bullet \left[\frac{2 \bullet \omega_{MeFo,r}}{M_{MeFo}} + \sum_{i=1}^{6} \left(\frac{i \bullet \omega_{OME_i,r}}{M_{OME_i}} \right) \right]^{-1} \tag{5}$$

Here, M_i is the molar mass of component i.

2.3. Experiments from a previous study

Experiments performed in a previous study from our group (Drexler et al. 2022) were also considered for the model development. These experiments were performed with of 20 g of reactants (DME + TRI) and 0.52 g of H-ZSM-5 (Si/Al = 40) in a 75 mL autoclave. No dilution with dodecane was used, which is the main difference between these experiments and the ones from the present work. The total reaction time was always 2 h including the heating ramp, and a liquid sample was collected at t = 2h to be analyzed by the GC. A total of 15 experiments were conducted, varying the final temperature (353–425 K) and the initial n_{TRI}/n_{DME} (0.10–1.00). Further information can be found in the original work (Drexler et al. 2022). Experiments with T > 400 K were not considered, as the OME selectivity is much lower (MeFo production rises), and even methanol was detected at these conditions.

3. Kinetic modeling

3.1. Reaction network

Trioxane (TRI) decomposes to formaldehyde (FA), as follows.

$$TRI \rightleftarrows 3 \bullet FA \tag{6}$$

OME is formed either by reaction of formaldehyde (FA) with DME (Eq. (7)) or by direct incorporation of TRI (Eq. (8)).

$$DME + FA \rightleftarrows OME_1 \tag{7}$$

$$DME + TRI \rightleftarrows OME_3 \tag{8}$$

While these two reactions might occur in parallel, it is not trivial to find statistically significant parameters for both pathways through parametrization. Therefore, it was considered that one reaction could satisfactorily describe OME formation, and two models were developed: Model A considers that OME formation occurs only via Eq. (7), while Model B considers only Eq. (8).

OME chain elongation is described in the literature both by the formaldehyde pool (Eq. (9)) and by transacetalization reactions (Eq. (10)) (Drexler et al., 2022).

$$OME_{n-1} + FA \rightleftarrows OME_n \tag{9}$$

$$OME_{n-1} + OME_m \rightleftarrows OME_n + OME_{m-1} \tag{10}$$

Since the OME chain elongation is generally faster than OME formation from DME (Breitkreuz et al., 2022b; Drexler et al., 2023), consideration of only one route in the model should be sufficient to describe this process. The formaldehyde pool was chosen because it consists of a lower number of reactions, it is simpler to implement and to define the equilibrium constants. Breitkreuz et al. (2022b) made the same choice to simulate the OME chain propagation.

The formation of MeFo is typically described by a Tishchenko-type reaction (Drexler et al., 2022) (Eq. (11)). An alternative pathway via OME_2 decomposition was proposed by Breitkreuz et al. (2022b) (Eq. (12)). In the present kinetic model, the more established Tishchenko reaction (Eq. (11)) was considered.

$$2 \bullet FA \rightarrow MeFo \tag{11}$$

$$OME_2 \rightarrow MeFo + DME \tag{12}$$

No other side products were detected in the operating conditions applied in this work, indicating that water contamination did not occur, and the process ran under dry conditions. Therefore, no other reactions were considered in the kinetic modeling. The reaction network is illustrated in Fig. 1.

Table 2
Reaction rate equations.

Reaction	Rate of reaction ($mol \cdot kg_{cat}^{-1} \cdot h^{-1}$)	No.
OME synthesis via FA (Eq. (6)) (Model A)	$r_1 = \frac{k_1}{1 + K_{Dod} \bullet a_{Dod}} \bullet \left(\sqrt[3]{a_{TRI}} \bullet a_{DME} - \frac{a_{OME_1}}{K_{P,1}} \right)$	(17)
OME synthesis via TRI (Eq. (7)) (Model B)	$r_1 = \frac{k_1}{1 + K_{Dod} \bullet a_{Dod}} \bullet \left(a_{TRI} \bullet a_{DME} - \frac{a_{OME_1}}{K_{P,1}} \right)$	(18)
OME chain elongation (Eq. (8)) (Models A and B)	$r_n = \frac{k_n}{1 + K_{Dod} \bullet a_{Dod}} \bullet \left(\sqrt[3]{a_{TRI}} \bullet a_{OME_{n-1}} - \frac{a_{OME_n}}{K_{P,n}} \right) 2 \le n \le 6$	(19)
MeFo formation (Eq. (10)) (Models A and B)	$r_7 = k_7 \bullet \sqrt[3]{a_{TRI}^2}$	(20)

3.2. Reaction rates

Following the approach of Breitkreuz et al. (2022b), a pseudo-homogeneous approach based on activities was considered. Thus, the reaction rate of trioxane decomposition (r_0, in $mol \cdot kg_{cat}^{-1} \cdot h^{-1}$) is:

$$r_0 = k_0 \bullet \left(a_{FA}^3 - \frac{a_{TRI}}{K_{P,0}} \right) \tag{13}$$

where k_0 is the reaction constant ($m^9 \cdot mol^{-2} \cdot kg_{cat}^{-1} \cdot h^{-1}$), a_i is the activity of component i ($mol \cdot m^{-3}$), and $K_{P,0}$ is the equilibrium constant ($m^6 \cdot mol^{-2}$).

No free FA was detected in the offline GC measurements, which is in agreement with the literature (Breitkreuz et al., 2022b; Drexler et al., 2023; Peláez et al., 2020) and makes it challenging to estimate the kinetics of TRI decomposition. Additionally, this reaction is described as fast in the OME synthesis from DME (Breitkreuz et al., 2022b). Therefore, TRI decomposition was considered rapid in this work, i.e. quasi-equilibrium was assumed. That is:

$$k_0 \gg r_0 \rightarrow \frac{r_0}{k_0} \approx 0 \tag{14}$$

$$a_{FA}^3 - \frac{a_{TRI}}{K_{P,0}} = 0 \tag{15}$$

$$a_{FA} = \sqrt[3]{\frac{a_{TRI}}{K_{P,0}}} \tag{16}$$

The reaction rate equations are summarized in Table 2. In these equations, the activity of FA is already substituted according to Eq. (16),

and the kinetic parameters were lumped to avoid the estimation of $K_{P,0}$. The OME chain length was limited to OME_6, since only traces of heavier OMEs were detected.

From preliminary tests it was observed that the OME formation was much slower when dodecane was present, which could not be explained/simulated correctly by dilution alone. Furthermore, for the experiments containing dodecane, it took longer for OME_1 and OME_2 to reach quasi-equilibrium through chain propagation. Dodecane is possibly causing some hinderance in these reactions, for which we have two hypotheses:

1. Dodecane is non-polar, while DME and TRI are polar, as is the surface of the zeolite. The presence of large amounts of dodecane inside the catalyst pores may affect the active sites and change the kinetics of OME synthesis.
2. Dodecane could cause steric hindrance for the arrangement of larger molecules inside the pores. This could affect the kinetics of OME synthesis and chain propagation, while MeFo production might remain unaffected, as both MeFo and formaldehyde are smaller molecules.

To account for this effect, an inhibition term $(1 + K_{Dod} \bullet a_{Dod})^{-1}$ was added to the reaction rates of both the OME production (Eqs. (17) and (18)) and chain propagation (Eq. (19)), where K_{Dod} is temperature dependent and calculated as follows:

$$K_{Dod} = K_{Dod,0} \bullet \exp\left[-\frac{B_{Dod}}{R} \bullet \left(\frac{1}{T} - \frac{1}{T_{ref}} \right) \right] \tag{21}$$

Activities were calculated with Eq. (21). The activity coefficients were estimated using a UNIFAC-based model with parameters from the literature (Breitkreuz et al., 2022b; Breitkreuz et al., 2023; Breitkreuz et al., 2018; Gmehling et al., 1982; Horstmann et al., 2005; Kuhnert, 2004; Schmitz et al., 2018) (see Section S2 of the SM).

$$a_i = \frac{n_{tot} \bullet (1 - v) \bullet x_i \bullet \gamma_i}{V_L} \tag{22}$$

where n_{tot} is the total number of moles considering both the liquid and gas phases, v is the vapor fraction in the system (mol in the gas phase/mol in total), x_i is the molar fraction of component i in the liquid phase, and V_L is the volume of the liquid phase (m^3).

The reaction constants were calculated according to an Arrhenius-type equation.

$$k_k = \exp\left[A_k - \frac{E_{A,k}}{R} \bullet \left(\frac{1}{T} - \frac{1}{T_{ref}} \right) \right] \tag{23}$$

Here, A_k is a lumped kinetic constant, $E_{A,k}$ is the activation energy ($kJ \cdot mol^{-1}$), R is the universal gas constant ($kJ \cdot mol^{-1} \cdot K^{-1}$), T is the reaction temperature, and T_{ref} is the reference temperature ($T_{ref} = 363.15$ K). The use of the reference temperature reduces the correlation between A_k and $E_{A,k}$, facilitating the parametrization process.

The reactions concerning the OME chain distribution (r_{2-6}) were considered rapid by Breitkreuz et al. (2022b) (system: OME_n synthesis from DME using ion-exchange resin as catalyst), while Peláez et al. (2020) made the same consideration with the exception of OME_2 formation from OME_1 (system: OME_n synthesis from OME_1 using an undisclosed commercial catalyst). In this work, following the literature approach, reactions r_{2-6} were considered rapid, and a sufficiently high constant value was applied, i.e. $k_{2-6} = 0.1\ m^4 \cdot mol^{(-1/3)} \cdot kg_{cat}^{-1} \cdot h^{-1}$.

Accurate values of the equilibrium constants ($K_{P,1-6}$) are not trivial to obtain for this system. This is because MeFo formation is slow and either irreversible or only equilibrates at very high MeFo concentration, thus preventing the system from reaching chemical equilibrium under typical reaction times, a fact that has been elucidated in the literature (Breitkreuz et al., 2022b). In the case of OME formation from DME (Eqs. (7) and (8)), its equilibrium constant ($K_{P,1}$) was fitted to the experimental database together with the kinetic constants. At first, an Arrhenius type equation was considered, i.e. $K_{P,k} = \exp(A_{eq,k} - B_{eq,k}/RT)$. The temperature dependent parameter (B) was found to be statistically insignificant and was therefore excluded, so that $K_{P,1}$ was fitted as a single parameter, i.e. $K_{P,1} = \exp(A_{eq,1}) = \text{constant}$.

To estimate the equilibrium constants of the OME chain elongation (Eq. (9)), we tested a three-parameter Schulz-Flory distribution correlation described by Peláez et al. (2020), which correlates $K_{P,2-6}$ with temperature and the chain length. However, the parameters were not statistically significant, indicating a low dependency of $K_{P,2-6}$ in relation to temperature and chain length in the operating conditions of the present study. Therefore, all equilibrium constants of the OME chain propagation were set equal and temperature-independent, decreasing the number of fitted parameters by two. That is: $K_{P,2-6} = \exp(A_{eq,2})$.

3.3. Vapor-liquid equilibrium

In this section, the procedure for estimating the vapor–liquid equilibrium conditions inside the reactor is described. To simulate the gas phase, both ideal gas and the predictive Soave-Redlich-Kwong (PSRK) (Breitkreuz et al., 2022b; Horstmann et al., 2005) approaches have been tested, with negligible difference in the results. There are probably two reasons for this: (i) low reactor pressure ($p < 15$ bar) and (ii) the mass of the gas phase was minimal compared to the liquid phase ($m_V/m_L \approx 0.006$), so that non-idealities in the gas phase would have negligible effects on the liquid phase, where the reaction takes place. Therefore, to reduce complexity and computational time, ideal gas behavior was chosen for the modeling.

To start the calculations, initial values for the vapor fraction (v) and the liquid composition (x_i) are required. For $t = 0$, initial values of $v = 0.01$ mol/mol and $x_i = z_i$ were used. z_i is defined as the mole fraction of component i considering both the liquid and gas phases, that is:

$$z_i = \frac{n_i}{n_{tot}} \tag{24}$$

Here, n_i is the number of moles of component i in both phases, and n_{tot} is the total number of moles inside the reactor.

For all other points in the time integration, v and x_i from the previous point were considered. With a defined x_i, the molar volume of the liquid phase (v_L, in $mol \cdot m^{-3}$) was estimated. Excess volumes were neglected.

$$v_L = v_{L,i} \bullet x_i \tag{25}$$

where $v_{L,i}$ is the molar volume of the pure component i.

The equation and the corresponding coefficients to estimate the temperature-dependent molar volume of pure components were obtained from the literature (Breitkreuz et al., 2022b; Burger et al., 2013; Haynes, 2014; Yamada and Gunn, 1973) and are available in the SM (see Section S3). The activity coefficients (γ_i), related to liquid–liquid interactions, were calculated at this point with the defined (x_i), using the UNIFAC-based model.

With v_L and γ_i defined, the iterative calculation of the vapor fraction (v) was started. First, the liquid volume (V_L, in m^3) and the gas volume (V_G, in m^3) were calculated.

$$V_L = v_L \bullet (1 - v) \bullet n_{tot} \tag{26}$$

$$V_G = V_R - V_L \tag{27}$$

Here, V_R is the reactor total inner volume.

Then, the reactor pressure (p) was calculated according to the ideal gas law.

$$p = \frac{v \bullet n_{tot} \bullet R \bullet T}{V_G} \tag{28}$$

The partition coefficients (K_i) were calculated for each component using the extended Raoult's law.

$$K_i = \exp\left[\frac{\left(p - p_{vap,i}\right) \bullet v_{L,i}}{R \bullet T}\right] \bullet \frac{\gamma_i \bullet p_{vap,i}}{p} \tag{29}$$

where $p_{vap,i}$ is the vapor pressure of component i at T. The equation and corresponding coefficients to estimate the vapor pressure of each component were taken from the literature (Breitkreuz et al., 2022a; Burger et al., 2013; Rowley et al., 2018; Willingham et al., 1945) and are available in the SM (see Section S4).

Finally, the flash equation must hold.

$$f = \sum_{i=1}^{N_{LC}} \left(\frac{z_i \bullet K_i}{1 - v + v \bullet K_i}\right) + \sum_{i=N_{LC}+1}^{N_C} \left(\frac{z_i}{v}\right) - 1 = 0 \tag{30}$$

Here, N_{LC} is the number of liquid phase components, and N_C is the total number of components. The second sum term refers to components that have negligible concentration in the liquid phase (i.e. $K_i \gg (1-v)/v$), i.e. nitrogen and oxygen.

Eqs. (26)–(30) were solved iteratively to find v such that $f = 0$. The Matlab function *fsolve* was used, with function and step tolerances set to 10^{-10}.

With the calculated v, the composition of the gas phase (y_i) and the liquid phase (x_i) are given by:

$$y_i = \frac{z_i \bullet K_i}{1 - v + v \bullet K_i} \tag{31}$$

$$x_i = \frac{y_i}{K_i} \tag{32}$$

The vapor–liquid equilibrium is recalculated at each time point because temperature and composition change with time. Since these changes are relatively slow and the reactor is continuously stirred, it was considered that the new vapor–liquid equilibrium is always immediately reached. In the next section, the reactor model including the time integration is described.

3.4. Reactor model

Since the substances in the batch reactor were thoroughly stirred, the heating ramp was relatively slow, and the reaction times were in the order of hours, the following considerations were made: (i) gradient-free reactor, (ii) no heat or mass transfer limitations, (iii) vapor–liquid equilibrium at all times. For a control volume containing the liquid and gas phases, the variation of the number of moles of each component i (n_i, in mol) along the reaction time (t, in h) is described according to the following equation.

$$\frac{dn_i}{dt} = m_{cat} \bullet \sum_{j=1}^{N_R} (v_{ik} \bullet r_k) \tag{33}$$

Here, m_{cat} is the total catalyst mass, and v_{ik} is the stoichiometric coefficient of component i in reaction k.

The heating program for each experiment consisted of two parts:

1. A heating ramp until the setpoint temperature (T_{SP}) was reached (normally after ca. 45 min).
2. Reaction at T_{SP} for several hours

The temperature profile was recorded for each case, and an empirical function were adjusted (Eq. (34)). The function coefficients are available in the SM (Section S5).

$$T(t) = A_T - B_T \bullet \exp(-C_T \bullet t) \tag{34}$$

where A_T, B_T, and C_T are adjusted parameters.

The reaction rates are negligible at lower temperatures (T < 338 K). In addition, mass transfer limitations may play a role before trioxane melts (at ca. 337 K). Therefore, any reaction at T < 338 K was neglected, and the time integration was performed only for t at $T \geq 338$ K. The system of ordinary differential equations (Eq. (33)) was solved with the Matlab function *ode45*, with the absolute tolerance set to 10^{-6} and the relative tolerance set to 10^{-4}. The function *ode45* was called twice:

1. To integrate Eq. (33) considering the temperature ramp (Eq. (34)) until the temperature setpoint is reached. The initial conditions are described in Table 1. For all components with $n = 0$ mol at the initial condition, a tiny value of 10^{-5} mol was assigned instead to avoid numerical instabilities caused by assigning zero in some cases.
2. To integrate Eq. (33) at constant temperature until the final reaction time. The final conditions of the 1st integration are used as initial conditions of the 2nd integration.

3.5. Estimation of the kinetic parameters

In total, 9 parameters (A_1, A_7, $E_{A,1}$, $E_{A,7}$, $K_{P,1}$, $K_{P,2-6,wD}$, $K_{P,2-6,nD}$ $K_{ad,0}$, ΔH_{ad}) were fitted to the experiments. In $K_{P,2-6,wD}$ and $K_{P,2-6,nD}$, *wD* and *nD* refer to "with dodecane" and "no dodecane", respectively. They were separately estimated because in preliminary simulations it was observed that a single value did not fit both situations. Further discussion about this is provided in Section 4.4.

From the database of the present work, experiments E1, E3-E8, and E10-12 were selected as the training database, while E2 and E9 were kept for validation only. From the database of our previous work (Drexler et al., 2022), points P2-P5 and P11-P13 were added to the training database.

An objective problem was solved following the chi-square regression method (χ^2), i.e. minimizing the sum of normalized squared deviations with respect to each OME and MeFo contents (Eq. (35)).

$$\chi^2 = \sum_{i=1}^{N_{TP1}+N_{TP2}} \left\{ w_{i,MeFo} \bullet \left(z_{i,MeFo} - \hat{z}_{i,MeFo}\right)^2 + \sum_{n=1}^{6} \left[w_{i,OME_n} \bullet \left(z_{i,OME_n} - \hat{z}_{i,OME_n}\right)^2 \right] \right\} \tag{35}$$

Here, N_{TP1} and N_{TP2} are the number of training points/measurements from this work and from (Drexler et al., 2023) ($N_{TP1} = 53$, $N_{TP2} = 7$), respectively, $z_{i,j}$ is the measured mole fraction of component j at measurement i, $\hat{z}_{i,j}$ is the simulated mole fraction of component j at point i, and $w_{i,j}$ is the weight of component j at point i.

The inverse values of the squared measured mole fractions were used as weights, provided that they were above a certain threshold (Eq. (36)). With this procedure, the optimization solver does not give too much weight to either the largest or the smallest values.

$$\begin{aligned} w_{i,j} &= \frac{1}{{z_{i,j}}^2} \quad for \quad z_{i,j} > 0.01 mol \Big/ mol \\ w_{i,j} &= 10^4 \quad for \quad z_{i,j} \leq 0.01 mol \Big/ mol \end{aligned} \tag{36}$$

The mean relative error related to each component, $MRE(j)$, was calculated considering both training and validation points, as follows.

$$MRE(j) = \frac{100\%}{(N_{TP1} + N_{TP2} + N_{VP})} \bullet \sum_{i=1}^{N_P} \frac{\left|z_{i,j} - \hat{z}_{i,j}\right|}{z_{i,j}} \tag{37}$$

where N_{VP} is the number of validation points ($N_{VP} = 11$).

To calculate the 95 % confidence interval of the fitted parameters, the Matlab function *nlparci* was used.

Table 3
Kinetic and equilibrium constants of Models A and B.

Parameter & χ^2 values	Model A	Model B
A_1 (−)	−8.56 ± 1.01	−13.97 ± 1.16
A_7 (−)	−4.70 ± 0.53	−4.71 ± 0.92
$E_{A,1}$ (kJ•mol^{-1})	59.42 ± 5.65	41.29 ± 7.80
$E_{A,7}$ (kJ•mol^{-1})	75.92 ± 8.64	78.39 ± 25.22
k_{2-6} (m^4·mol$^{(-1/3)}$·kg$_{cat}^{-1}$·h^{-1})	0.1*	0.1*
$K_{P,1}$	(4.09 ± 0.51)·10^{-3} (m•mol$^{-1/3}$)	(5.40 ± 0.66)·10^{-6} (m^3•mol^{-1})
$K_{P,2-6,wD}$ (m•mol$^{-1/3}$) (with dodecane)	(2.39 ± 0.30)·10^{-2}	(2.39 ± 0.80)·10^{-2}
$K_{P,2-6,nD}$ (m•mol$^{-1/3}$) (no dodecane)	(1.68 ± 1.17)·10^{-2}	(1.68 ± 0.47)·10^{-2}
$K_{Dod,0}$ (m^3•mol^{-1})	(1.04 ± 0.09)·10^{-2}	(2.83 ± 0.52)·10^{-3}
B_{Dod} (kJ•mol^{-1})	−0.85 ± 0.09	−102.84 ± 58.15

* High values arbitrarily chosen, as these reactions were considered to be in quasi-equilibrium.

Table 4
Statistical indicators of kinetic models A and B.

Indicators	Model A	Model B
χ^2 − ***Training***	29.9	14.4
χ^2 − ***Training*** + ***E2 and E9***	32.9	16.3
MRE(***OME***$_1$)	27.4	17.5
MRE(***OME***$_2$)	26.1	13.0
MRE(***OME***$_3$)	25.5	14.7
MRE(***OME***$_4$)	27.3	19.2
MRE(***OME***$_5$)	34.4	25.5
MRE(***OME***$_6$)	49.6	42.4
MRE(***OME***$_{sum}$)	25.9	13.8
MRE(***MeFo***)	27.1	25.2

4. Results and discussion

The experimental results are provided in the SM (Section S1). No OME or MeFo was detected in E13 (blank experiment), excluding the possibility of reactions occurring without the presence of a catalyst within the studied operating range (T ≤ 393 K).

4.1. Parameter estimation and model validation

The kinetic and equilibrium parameters of Models A and B are presented in Table 3, while the statistical indicators of both models are summarized in Table 4. The confidence intervals show that all parameters are statistically significant for both models.

The χ^2 of Model B is ca. 50 % lower than of Model A, suggesting that direct trioxane incorporation to form OME_3 (Model B) is the main reaction pathway of OME formation. While this result does not exclude the possibility that OME formation also occurs by reaction of FA and DME, it supports the hypothesis that direct trioxane incorporation to OME_3 is much faster than OME_1 formation from DME and FA. This result contrasts the one from Breitkreuz et al. (2022b), who obtained similar results with both approaches. However, the authors worked with a different catalyst, an acidic ion-exchange resin, and the reaction mechanism may differ from the reaction mechanism on the H-ZSM-5.

Model B simulates the total OME production with a mean error of only 13.8 %, while the predictions of the individual OME fractions and MeFo have mean deviations ranging between 13.0 and 25.5 %, except for OME_6, whose higher deviations are associated with higher measurement errors, caused by the low concentrations of these components.

Since Model B describes the experiments much better than Model A, the further discussion focuses on Model B. In Fig. 2, parity plots of OME and MeFo concentration are shown for Model B simulations. Analogous parity plots for Model A simulations are provided in the SM (Section S6). Although Model B has a low number of fitted parameters (9) for a high number of products (7), OME formation and MeFo side production were adequately simulated without systematic deviations, and similar accuracy was observed for the validation points.

4.2. Influence of temperature

The effect of temperature in OME synthesis is shown in Fig. 3 (experiments with dodecane) and Fig. 4 (experiments without dodecane).

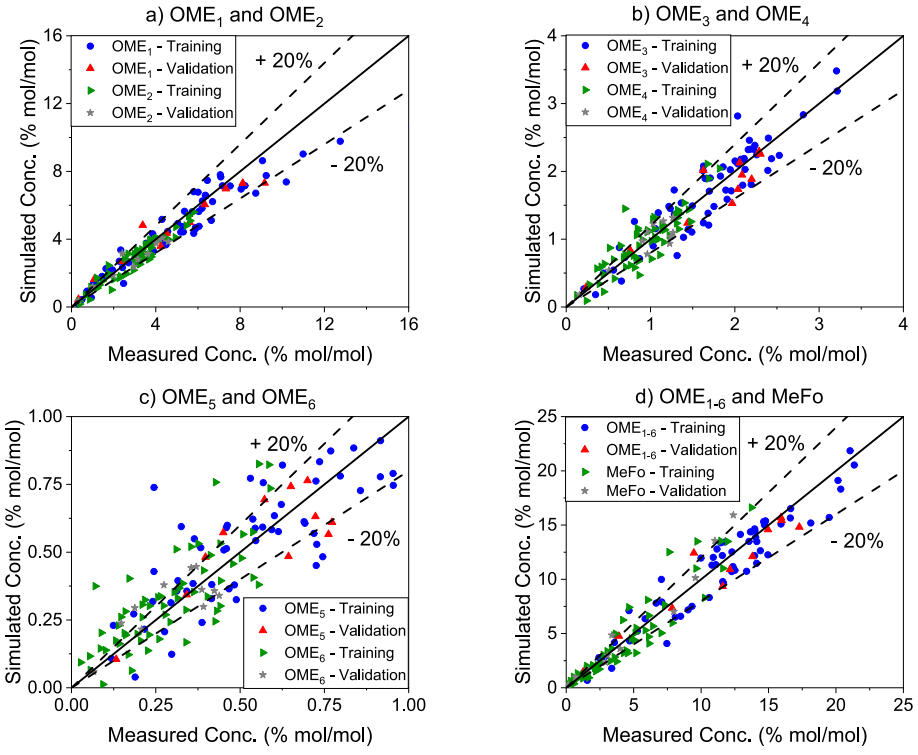

Fig. 2. Simulations of Model B vs. measurements. a) OME_1 and OME_2. b) OME_3 and OME_4. c) OME_5 and OME_6. d) Sum of OME_{1-6}, and MeFo.

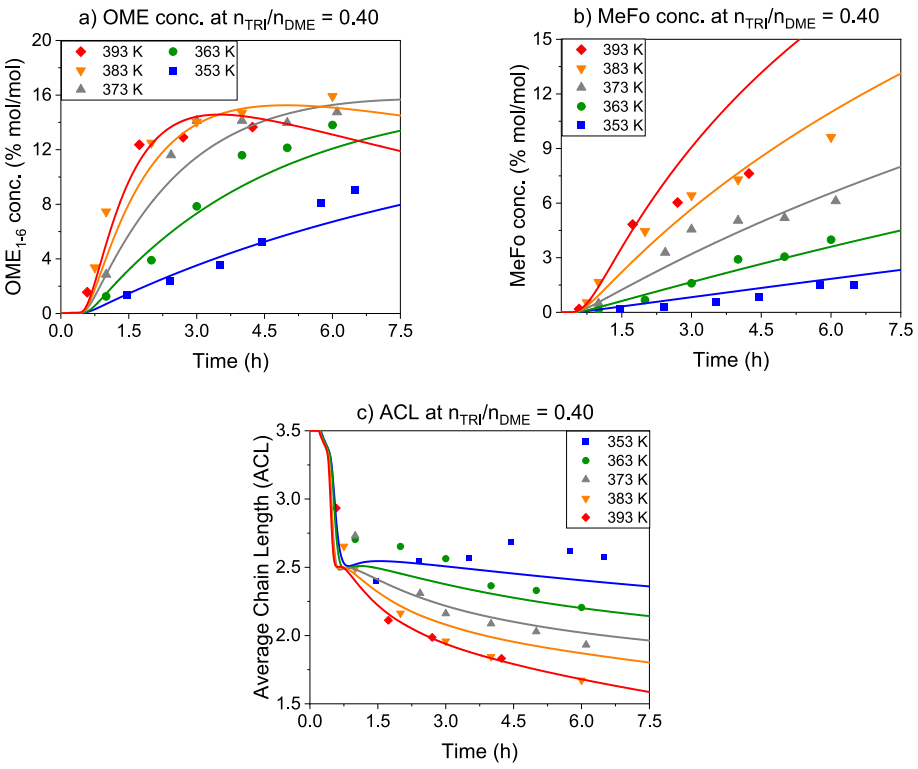

Fig. 3. Effect of temperature in the OME synthesis for experiments containing dodecane. The dots represent the measurements (E1-E5), and the curves refer to Model B simulations. a) OME_{1-6} concentration (% mol/mol), b) MeFo concentration (% mol/mol), c) Average Chain Length (ACL).

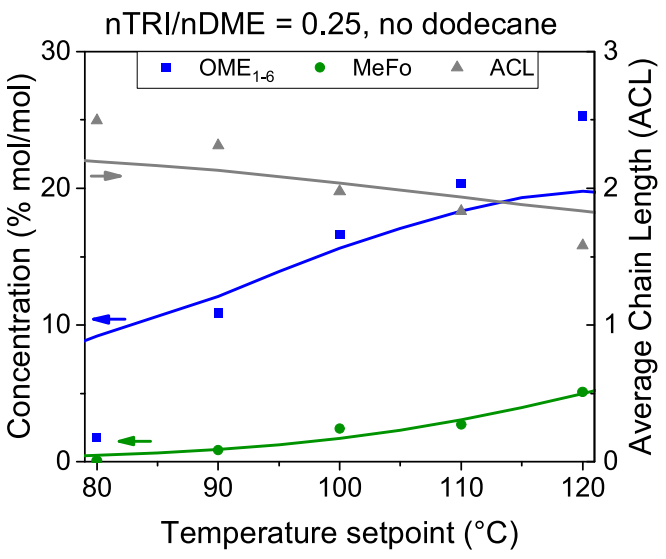

Fig. 4. Effect of temperature in the OME synthesis for experiments without dodecane. The dots represent the measurements (P1-P5), and the curves refer to Model B simulations. The reaction time is 2 h for all points.

Increasing temperature promotes both OME and MeFo production (see Figs. 3a, b, and 4), but decreases OME selectivity, in agreement with the literature (Burre et al., 2019; Haltenort et al., 2018; Liu et al., 2019). After a few hours of reaction, MeFo production continues to increase (Fig. 3b), while OME generation seems to reach a plateau (at higher temperatures), i.e. the chemical equilibrium has been reached (Fig. 3a).

In the experiment without dodecane at 353 K (P1, Fig. 4), high overestimations of both OME and MeFo production were observed. Since the temperature influence was correctly simulated for 363 – 393 K (P2-P5, Fig. 4a), as well as for the experiment with dodecane at 353 K (E1, Fig. 3a and b), we suspect that some experimental error might have occurred with P1, e.g. GC measurement errors are higher at low concentrations. In general, while there were some discrepancies between measurements and simulations, the kinetic model accurately simulated the experimental trends of the data with and without dodecane.

A typical indicator of chain growth is the average chain length (ACL). It is calculated as follows (Drexler et al., 2023).

$$ACL = \sum_{i=1}^{6} \left(i \bullet z_{OME_i,r}\right) \bullet \left[\sum_{i=1}^{6} \left(z_{OME_i,r}\right)\right]^{-1} \quad (38)$$

The effect of temperature on the ACL is shown in Fig. 3c. The ACL decreases with reaction time and by increasing the temperature, as shown in previous studies (Drexler et al., 2022; Drexler et al., 2023). Model B correctly predicted the experimental trend for both cases (with and without dodecane), while slight underestimations were observed at lower temperatures and short reaction times. The cause of these underestimations may be related to considering the OME chain distribution to be in quasi-equilibrium, since the generation of OME_1 and OME_2 from OME_3 may not be as fast at lower temperatures. Nevertheless, the current approach was maintained, because (i) the deviations are small and occur only at specific points, and (ii) we did not obtain statistically significant kinetic parameters for the OME chain distribution when including them in the model.

4.3. *Influence of the initial composition*

The effect of initial composition on the OME synthesis is shown in Fig. 5 (experiments with dodecane) and Fig. 6 (experiments without dodecane). By increasing the TRI/DME ratio, MeFo production increases considerably (see Figs. 5c–f and 6), while the OME formation reaches a maximum for nTRI/nDME between 0.40 and 0.55, although close results are also obtained for nTRI/nDME = 0.25 and 0.70 (see Figs. 5a, , and 6).

At 383 K, the plateau in OME production was reached for all cases (Fig. 5b), suggesting a proximity to the chemical equilibrium, and this

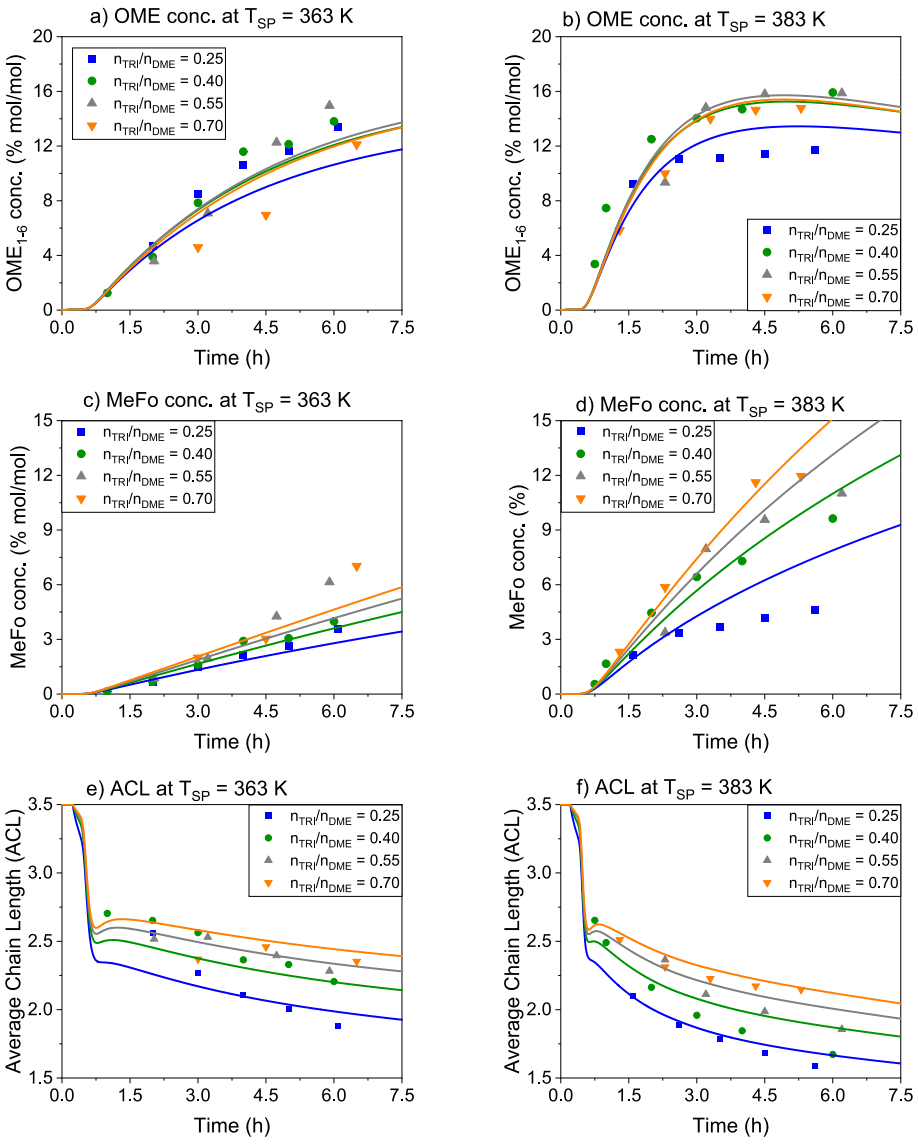

Fig. 5. Effect of the initial composition (i.e. n_{TRI}/n_{DME}) in the OME synthesis for experiments containing dodecane. The dots represent the measurements (at 363 K: E2, E6, E8, E10; at 383 K: E4, E7, E9, E11), and the curves refer to Model B simulations. a and b) Total OME concentration (% mol/mol), c and d) MeFo concentration (% mol/mol), e and f) Average Chain Length (ACL).

plateau is slightly higher with an increase in the TRI/DME ratio. As expected, increasing the TRI/DME ratio leads to longer OME chains, i.e. higher ACL (see Fig. 5e, f, and 6). In summary, there is a trade-off between OME selectivity and ACL, with increasing TRI worsening the former and improving the latter.

The model follows the experimental trends and accurately reproduces most experimental points, and low deviations are seen at specific conditions in the experiments with dodecane. Significant overestimations are observed for very low (nTRI/nDME = 0.10) as well as very high trioxane content (nTRI/nDME > 0.85) in the experiments without dodecane (see Fig. 6). These points did not participate in the model training, as these operating regions are not the most interesting, since catalyst performance is reduced. At very low TRI content, one hypothesis for the overestimation is that DME could be saturating the catalyst surface at such high concentrations, consequently decreasing OME production rate, what is not considered by the kinetic model. At very high TRI content, one possible explanation for the overestimations is that TRI solubility issues might start to play a role, a phenomenon not included in the model.

4.4. OME chain distribution

The concentration of each OME_n over time is illustrated in Fig. 7 (selected experiments with dodecane) and Fig. 8 (experiments without dodecane). The consideration of a rapid OME chain elongation and the averaged equilibrium constant was sufficient to capture the trends in the OME distribution, with low deviations at specific points, especially for OME_1. This is shown for variations in temperature (Figs. 7a–c, and 8a), feed composition (Figs. 7b, d–e, and 8b), and dodecane amount (Fig. 7b and f).

In the first measured samples of the experiments at lower temperatures ($T \leq 363.15$ K), the concentrations of OME_1 and OME_2, sometimes even OME_3, are close to each other (Fig. 7). These observations support that: (i) at lower temperature and low conversion, the OME chain distribution is not fully equilibrated in the first hours of the reaction; and (ii) OME production should occur primarily via direct trioxane incorporation to OME_3 (Eq. (8)), since these higher OME_2 and OME_3 concentrations would not be possible if OME production proceeded exclusively via OME_1 formation (Eq. (7)).

These observations suggest that the kinetic parameters from r_2

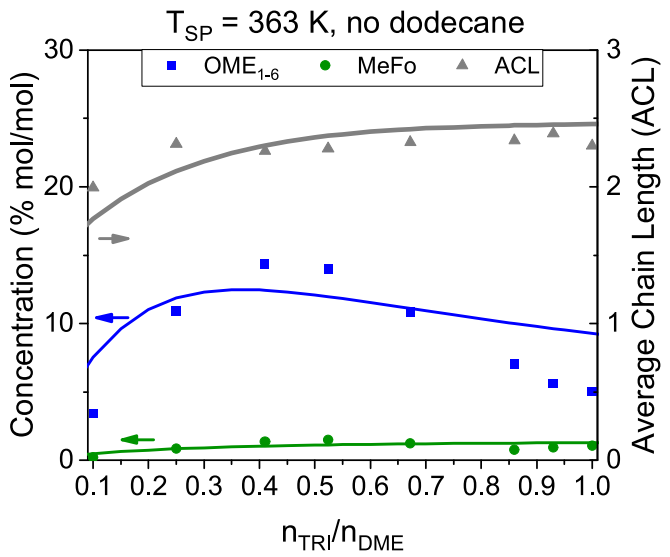

Fig. 6. Effect of the initial composition (i.e. n_{TRI}/n_{DME}) in the OME synthesis for experiments without dodecane. The dots represent the measurements (P9–P16), and the curves refer to Model B simulations.

($OME_1 + FA \rightleftarrows OME_2$) and possibly r_3 ($OME_2 + FA \rightleftarrows OME_3$) have slightly lower values than those of the subsequent reaction steps. However, as also concluded in Section 4.2, this effect is limited and has little relevance for practical applications. In the experiments without dodecane, this effect is even less pronounced. Thereby, the consideration of quasi-equilibrium for all reactions in the OME chain elongation was maintained.

As mentioned in Section 3.5, a single equilibrium constant was not sufficient to match the experiments with and without dodecane. When looking at Figs. 7 and 8, one can see that the OME concentrations are further from each other when no dodecane is in the system, suggesting that the addition of dodecane favors higher OME chains. Our hypothesis for the model mismatch with a single equilibrium constant value is that: when dodecane is added, the activity of all components is changed, but since there are some missing values in the UNIFAC binary interaction parameters, it is possible that this change is not fully captured by the model. However, when adjusting one constant for each situation (with and without dodecane), accurate simulations were obtained.

4.5. Conceptual design of a continuous OME_{3-4} production process

Stroefer et al. (2011) filed a patent on a process for the continuous production of OME from TRI and dialkyl ethers, whose flowsheet basically consisted of a fixed-bed reactor and two distillation columns. Later on, Breitkreuz et al. (2018) simulated and optimized this process specifically for TRI and DME, though not including MeFo side production. In this section, a new concept design is proposed, taking into account the side production of MeFo, and aiming to produce OME_{3-4} from DME and TRI.

The experimental and modeling results indicate that there is a compromise between high OME selectivity (low MeFo side production), high ACL and reasonable catalyst activity. Considering that, the best operating temperature for the conversion of DME to OME should be between 353 and 363 K, while the best feed composition should be between $n_{TRI}/n_{DME} = 0.25$ and 0.40.

Although a high ACL is desired in the first step, it is known that OME chain growth can occur at lower temperatures ($T \leq 333$ K) (Peláez et al., 2020), minimizing or even completely avoiding MeFo side production. Therefore, a continuous production plant with two fixed-bed tubular reactors would efficiently produce the desired OME_{3-4} with reduced MeFo side production. The proposed flowsheet is illustrated in Fig. 9.

Initially, DME and TRI are mixed with the recycle stream and fed into the first reactor, the DME activator (pressurized, 353 K $\leq T \leq$ 363 K, $0.25 \leq n_{TRI}/n_{DME} \leq 0.40$). After the reaction, unreacted DME is separated from the product stream in a pressurized column and recycled. The remaining product stream enters a pressure relief valve, because the second plant section can be operated at lower pressures (perhaps even atmospheric), minimizing equipment and operating costs. Important considerations to select the operating pressure of the first section are:

i. The pressure should be high enough to ensure liquid DME in the reactor, but low enough to avoid the solidification of larger OME chains.
ii. The pressure should be sufficient to facilitate the separation of DME and MeFo (Column 1) by allowing the condenser to be operated with cooling water.
iii. The pressure should be as low as possible to minimize equipment and compression costs.

In the second section, additional TRI is mixed with the remaining product stream from the first reactor, and the resulting stream enters the second reactor (low or atmospheric pressure, T $\leq$ 333 K). Since full conversion is not possible due to the chemical equilibrium constraints, separation via distillation columns and recycle streams of trioxane, OME_{1-2}, and $OME_{n\geq5}$ is required.

Theoretically, there are three possible positions for Column 2: (i) after Reactor 1, (ii) after the pressure valve, (iii) after Reactor 2. Since MeFo is inert in Reactor 2, and the concentration of OME_1 (volatile compound) is much lower after the second reactor, option (iii) is probably the most appropriate, allowing a more efficient separation of MeFo from the product stream and removing (possible) MeFo produced in the second reactor.

5. Conclusions

In this work, a new kinetic model was developed and accurately simulated the OME synthesis from dimethyl ether (DME) and trioxane (TRI). While both the direct OME_3 production from TRI and the OME_1 production from formaldehyde should occur in parallel, the experiments were better described when the former reaction was considered, supporting the hypothesis that the direct TRI incorporation into OME_3 is the main reaction pathway for OME formation on H-ZSM-5. The developed model is suitable for scale-up and optimization purposes.

A good compromise between catalyst activity and OME selectivity was found by operating at lower temperatures (353 K $\leq T \leq$ 363 K) and low TRI content ($0.25 \leq n_{TRI}/n_{DME} \leq 0.40$), where an OME selectivity around 90 % m/m can be achieved. These findings were used to propose a process concept for the continuous large-scale production of OME_{3-4} from DME and TRI. Two sections were considered: (i) a DME activation section, where the reactor operates at moderate pressures and the aforementioned conditions, and (ii) an OME chain growth section, which can be operated at lower pressures and temperatures, minimizing MeFo formation and reducing costs.

Both DME and TRI can be produced from methanol. Provided that green methanol from renewable resources is used, sustainable process chains with minimized overall emissions and high efficiency can be developed. The presented results can contribute to such strategy in terms of an optimized OME production with high selectivity towards the desired fractions, according to the projected applications.

CRediT authorship contribution statement

Bruno Lacerda de Oliveira Campos: Writing – original draft, Visualization, Validation, Software, Methodology, Formal analysis, Data curation, Conceptualization. **Philipp Beeskow:** Writing – review & editing, Software, Methodology, Investigation, Formal analysis, Data curation, Conceptualization. **Marius Drexler:** Writing – review &

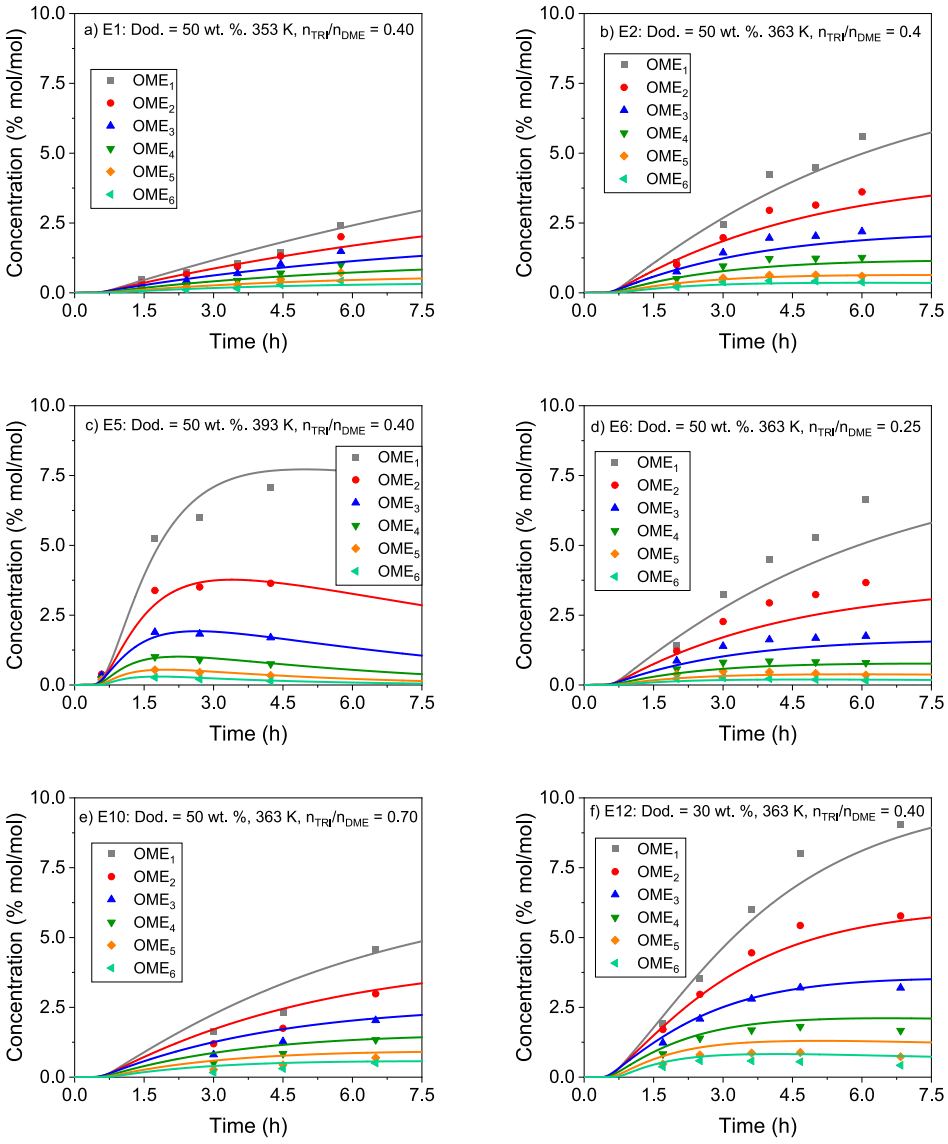

Fig. 7. OME_n concentration along time – Experimental measurements (dots) and Model B simulation (curves) for experiments with dodecane. a) E1. b) E2. c) E5. d) E6. e) E10. f) E12.

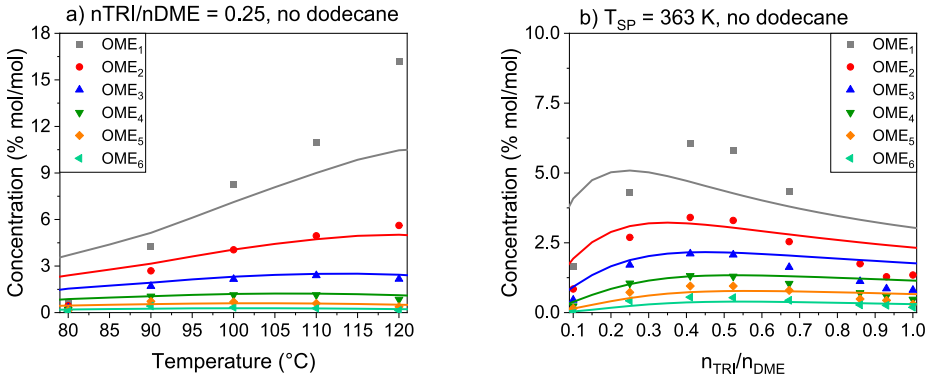

Fig. 8. OME_n concentration along time – Experimental measurements (dots) and Model B simulation (curves) for experiments without dodecane. a) Temperature variation for n_{TRI}/n_{DME} = 0.25 (P1–P5). b) n_{TRI}/n_{DME} variation for T_{SP} = 363 K (P9–P16).

editing, Methodology, Investigation, Data curation, Conceptualization. **Karla Herrera Delgado:** Writing – review & editing, Supervision. **Ulrich Arnold:** Writing – review & editing, Supervision, Resources, Project administration, Funding acquisition. **Jörg Sauer:** Writing – review & editing, Supervision, Project administration, Funding acquisition.

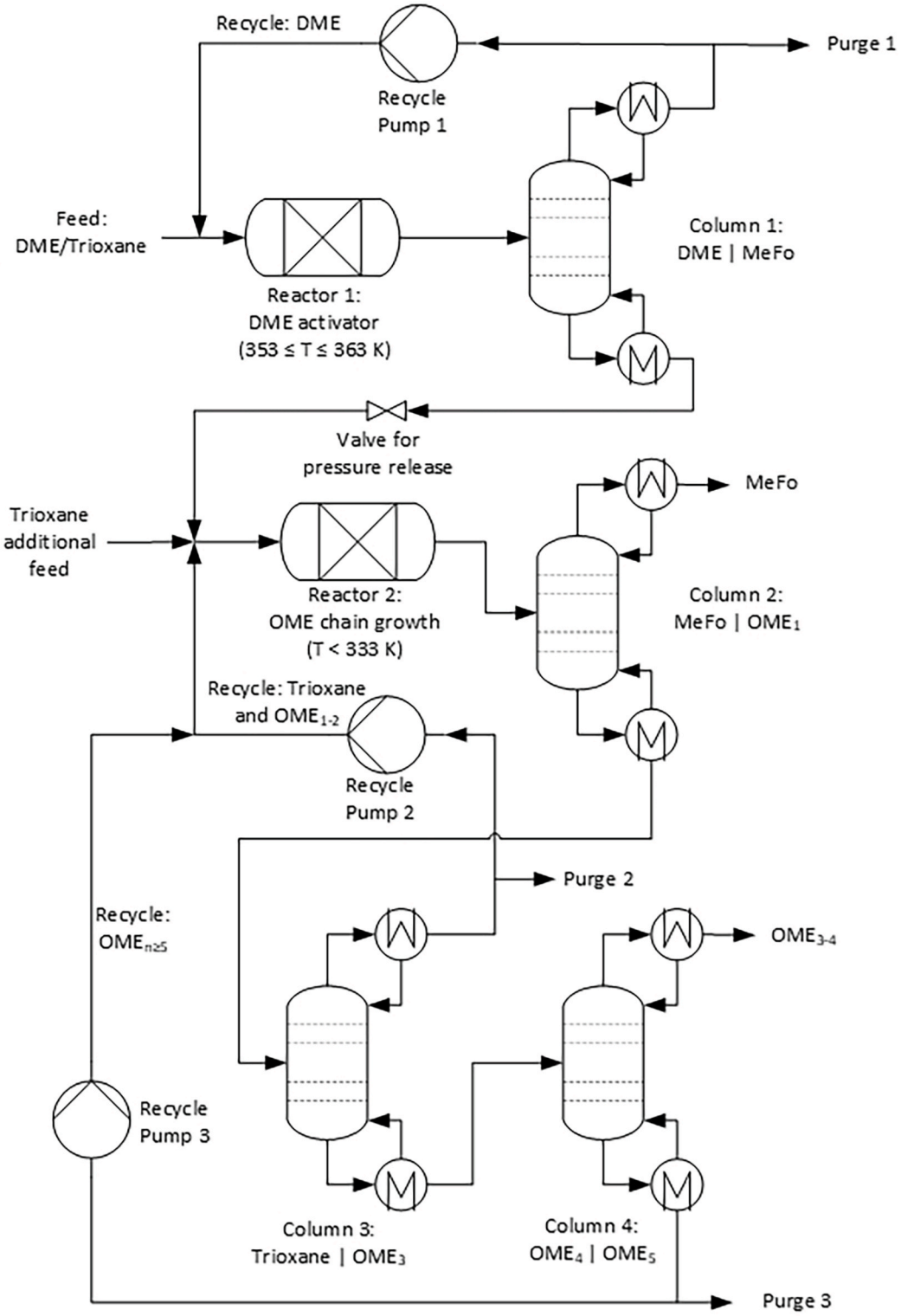

Fig. 9. Proposed conceptual design for OME_{3-4} production from DME and TRI. For each distillation column, the light key and heavy key components are given.

Declaration of competing interest

The authors declare that they have no known competing financial interests or personal relationships that could have appeared to influence the work reported in this paper.

Acknowledgments

The authors acknowledge the financial support from the Bundesministerium für Bildung und Forschung (BMBF) within the NAMOSYN Project (FKZ 03SF0566K0). The authors thank Zeolyst International for providing the zeolite catalyst.

Appendix A. Supplementary data

Supplementary data to this article can be found online at https://doi.org/10.1016/j.ces.2025.121655.

Data availability

Data will be made available on request.

References

An, G., Xia, Y., Xue, Z., Shang, H., Cui, S., Lu, C., 2022. Combination of theoretical and experimental insights into the oxygenated fuel poly(oxymethylene) dibutyl ether from n-butanol and paraformaldehyde. ACS Omega 7, 3064–3072.

Baranowski, C.J., Fovanna, T., Roger, M., Signorile, M., McCaig, J., Bahmanpour, A.M., Ferri, D., Kröcher, O., 2020. Water inhibition of oxymethylene dimethyl ether synthesis over zeolite H-beta: a combined kinetic and in situ ATR-IR study. ACS Catal. 10, 8106–8119.

Bartholet, D.L., Arellano-Treviño, M.A., Chan, F.L., Lucas, S., Zhu, J., St. John, P.C., Alleman, T.L., McEnally, C.S., Pfefferle, L.D., Ruddy, D.A., Windom, B., Foust, T.D., Reardon, K.F., 2021. Property predictions demonstrate that structural diversity can improve the performance of polyoxymethylene ethers as potential bio-based diesel fuels. Fuel 295, 120509.

Billion, A., Schulte, J., Vogel, A., Hilfinger, F., Krossing, I., 2024. Continuous anhydrous synthesis of oxymethylene dimethyl ethers by reaction of dimethyl ether with molecular formaldehyde. Small 20, 2306862.

Breitkreuz, C.F., Dyga, M., Forte, E., Jirasek, F., de Bont, J., Wery, J., Grützner, T., Burger, J., Hasse, H., 2022a. Conceptual design of a crystallization-based trioxane production process. Chem. Eng. Process. – Process Intesif. 171, 108710.

Breitkreuz, C.F., Hevert, N., Schmitz, N., Burger, J., Hasse, H., 2022b. Synthesis of methylal and poly(oxymethylene) dimethyl ethers from dimethyl ether and trioxane. Ind. Eng. Chem. Res. 61, 7810–7822.

Breitkreuz, C.F., Holzer, A., Fuchs, T., Günthner, M., Hasse, H., 2023. Miscibility in systems containing (poly(oxymethylene) ethers (OME) + hydrocarbons + water). Fuel 338, 127337.

Breitkreuz, C.F., Schmitz, N., Ströfer, E., Burger, J., Hasse, H., 2018. Design of a production process for poly(oxymethylene) dimethyl ethers from dimethyl ether and trioxane. Chem. Ing. Tech. 90, 1489–1496.

Burger, J., Ströfer, E., Hasse, H., 2013. Production process for diesel fuel components poly(oxymethylene) dimethyl ethers from methane-based products by hierarchical optimization with varying model depth. Chem. Eng. Res. Des. 91, 2648–2662.

Burre, J., Bongartz, D., Mitsos, A., 2019. Production of oxymethylene dimethyl ethers from hydrogen and carbon dioxide—part II: modeling and analysis for OME3–5. Ind. Eng. Chem. Res. 58, 5567–5578.

Deutsch, D., Oestreich, D., Lautenschütz, L., Haltenort, P., Arnold, U., Sauer, J., 2017. High purity oligomeric oxymethylene ethers as diesel fuels. Chem. Ing. Tech. 89, 486–489.

Drexler, M., Haltenort, P., Arnold, U., Sauer, J., 2022. Continuous synthesis of oxymethylene ether fuels from dimethyl ether in a heterogeneously catalyzed liquid phase process. Chem. Ing. Tech. 94, 256–266.

Drexler, M., Haltenort, P., Arnold, U., Sauer, J., Karakoulia, S.A., Triantafyllidis, K.S., 2023. Progress in the anhydrous production of oxymethylene ethers (OME) as a renewable diesel fuel in a liquid phase process. Catal. Today 424, 113847.

Drexler, M., Haltenort, P., Zevaco, T.A., Arnold, U., Sauer, J., 2021. Synthesis of tailored oxymethylene ether (OME) fuels via transacetalization reactions. Sustain. Energy Fuels 5, 4311–4326.

Gelner, A.D., Rothe, D., Kykal, C., Irwin, M., Sommer, A., Pastoetter, C., Härtl, M., Jaensch, M., Wachtmeister, G., 2022. Particle emissions of a heavy-duty engine fueled with polyoxymethylene dimethyl ethers (OME). Environ. Sci.: Atmos. 2, 291–304.

Gmehling, J., Rasmussen, P., Fredenslund, A., 1982. Vapor-liquid equilibriums by UNIFAC group contribution. Revision and extension. 2. Ind. Eng. Chem. Process Des. Dev. 21, 118–127.

Haltenort, P., Hackbarth, K., Oestreich, D., Lautenschütz, L., Arnold, U., Sauer, J., 2018. Heterogeneously catalyzed synthesis of oxymethylene dimethyl ethers (OME) from dimethyl ether and trioxane. Catal. Commun. 109, 80–84.

Härtl, M., Seidenspinner, P., Wachtmeister, G., Jacob, E., 2014. Synthetic diesel fuel OME1 a pathway out of the soot-NOx trade-off. MTZ Worldwide 75, 48–53.

Haynes, W.M., 2014. CRC Handbook of Chemistry and Physics, Section 3 – Physical Constants of Organic Compounds. CRC Press, Boca Raton.

Holzer, A., Günthner, M., Jung, P., 2022. Performance of pure OME and various HVO–OME fuel blends as alternative fuels for a diesel engine. Automot. Engine Technol. 7, 369–383.

Horstmann, S., Jabłoniec, A., Krafczyk, J., Fischer, K., Gmehling, J., 2005. PSRK group contribution equation of state: comprehensive revision and extension IV, including critical constants and α-function parameters for 1000 components. Fluid Phase Equilib. 227, 157–164.

Kuhnert, C., 2004. Dampf-Flüssigkeits-Gleichgewichte in mehrkomponentigen formaldhydhaltigen Systemen. Shaker Verlag, Aachen.

Liu, H., Wang, Z., Zhang, J., Wang, J., Shuai, S., 2017. Study on combustion and emission characteristics of Polyoxymethylene Dimethyl Ethers/diesel blends in light-duty and heavy-duty diesel engines. Appl. Energy 185, 1393–1402.

Liu, Y., Wang, Y., Cai, W., 2019. A synthesis, process optimization, and mechanism investigation for the formation of polyoxymethylene dimethyl ethers. Trans. Tianjin Univ. 25, 1–8.

Lucas, S.P., Chan, F.L., Fioroni, G.M., Foust, T.D., Gilbert, A., Luecke, J., McEnally, C.S., Serdoncillo, J.J.A., Zdanowicz, A.J., Zhu, J., Windom, B., 2022. Fuel properties of oxymethylene ethers with terminating groups from methyl to butyl. Energy Fuel 36, 10213–10225.

Maier, T., Härtl, M., Jacob, E., Wachtmeister, G., 2019. Dimethyl carbonate (DMC) and Methyl Formate (MeFo): emission characteristics of novel, clean and potentially CO2-neutral fuels including PMP and sub-23 nm nanoparticle-emission characteristics on a spark-ignition DI-engine. Fuel 256, 115925.

Mantei, F., Schwarz, C., Elwalily, A., Fuchs, F., Pounder, A., Stein, H., Kraume, M., Salem, O., 2023. A novel process towards the industrial realization of large-scale oxymethylene dimethyl ether production – COMET. React. Chem. Eng. 8, 2876–2893.

Oestreich, D., Lautenschütz, L., Arnold, U., Sauer, J., 2018. Production of oxymethylene dimethyl ether (OME)-hydrocarbon fuel blends in a one-step synthesis/extraction procedure. Fuel 214, 39–44.

Omari, A., Heuser, B., Pischinger, S., Rüdinger, C., 2019. Potential of long-chain oxymethylene ether and oxymethylene ether-diesel blends for ultra-low emission engines. Appl. Energy 239, 1242–1249.

Ouda, M., Yarce, G., White, R.J., Hadrich, M., Himmel, D., Schaadt, A., Klein, H., Jacob, E., Krossing, I., 2017. Poly(oxymethylene) dimethyl ether synthesis – a combined chemical equilibrium investigation towards an increasingly efficient and potentially sustainable synthetic route. React. Chem. Eng. 2, 50–59.

Peláez, R., Marín, P., Ordóñez, S., 2020. Synthesis of poly(oxymethylene) dimethyl ethers from methylal and trioxane over acidic ion exchange resins: a kinetic study. Chem. Eng. J. 396, 125305.

Pélerin, D., Gaukel, K., Härtl, M., Jacob, E., Wachtmeister, G., 2020. Potentials to simplify the engine system using the alternative diesel fuels oxymethylene ether OME1 and OME3−6 on a heavy-duty engine. Fuel 259, 116231.

Rowley, R.L., Wilding, W.V., Oscarson, J.L., Yang, Y., Zundel, N.A., Daubert, T.E., Danner, P., 2018. The DIPPR information and data evaluation manager for the design institute for physical properties, AIChE.

Schmitz, N., Breitkreuz, C.F., Ströfer, E., Burger, J., Hasse, H., 2018. Vapor–liquid equilibrium and distillation of mixtures containing formaldehdye and poly (oxymethylene) dimethyl ethers. Chem. Eng. Process. – Process Intesif. 131, 116–124.

Stroefer, E., Schelling, H., Hasse, H., Blagov, S., 2011. Method for the production of polyoxymethylene dialkyl ethers from trioxan and dialkylethers. US7999140 B2.

Voggenreiter, J., Burger, J., 2021. Side products in the water-tolerant synthesis of poly (oxymethylene) dimethyl ethers: formation kinetics and implications for process design. Ind. Eng. Chem. Res. 60, 2418–2429.

Voggenreiter, J., Ferre, A., Burger, J., 2022. Scale-up of the continuous production of poly(oxymethylene) dimethyl ethers from methanol and formaldehyde in tubular reactors. Ind. Eng. Chem. Res. 61, 10034–10046.

Willingham, C.B., Taylor, W.J., Pignocco, J.M., Rossini, F.D., 1945. Vapor pressures and boiling points of some paraffin, alkylcyclopentane, alkylcyclohexane, and alkylbenzene hydrocarbons. J. Res. Nat. Bur. Stand. 35, 219–244.

Yamada, T., Gunn, R.D., 1973. saturated liquid molar volumes. Rackett equation. J. Chem. Eng. Data 18, 234–236.